

# Insights into the activity of single-atom Fe-N-C catalysts for oxygen reduction reaction

Kang Liu<sup>1,2</sup>, Junwei Fu<sup>1</sup>, Yiyang Lin<sup>1</sup>, Tao Luo<sup>1</sup>, Ganghai Ni<sup>1</sup>, Hongmei Li<sup>1</sup>, Zhang Lin<sup>2</sup> & Min Liu<sup>1</sup>  

Single-atom Fe-N-C catalysts has attracted widespread attentions in the oxygen reduction reaction (ORR). However, the origin of ORR activity on Fe-N-C catalysts is still unclear, which hinder the further improvement of Fe-N-C catalysts. Herein, we provide a model to understand the ORR activity of Fe-N<sub>4</sub> site from the spatial structure and energy level of the frontier orbitals by density functional theory calculations. Taking the regulation of divacancy defects on Fe-N<sub>4</sub> site ORR activity as examples, we demonstrate that the hybridization between Fe 3d<sub>z<sup>2</sup></sub>, 3d<sub>yz</sub> (3d<sub>xz</sub>) and O<sub>2</sub> π\* orbitals is the origin of Fe-N<sub>4</sub> ORR activity. We found that the Fe-O bond length, the d-band center gap of spin states, the magnetic moment of Fe site and \*O<sub>2</sub> as descriptors can accurately predict the ORR activity of Fe-N<sub>4</sub> site. Furthermore, these descriptors and ORR activity of Fe-N<sub>4</sub> site are mainly distributed in two regions with obvious difference, which greatly relate to the height of Fe 3d projected orbital in the Z direction. This work provides a new insight into the ORR activity of single-atom M-N-C catalysts.

<sup>1</sup>Hunan Joint International Research Center for Carbon Dioxide Resource Utilization, School of Physics and Electronics, Central South University, Changsha 410083 Hunan, P. R. China. <sup>2</sup>School of Metallurgy and Environment, Central South University, Changsha 410083 Hunan, P. R. China.  
✉email: [minliu@csu.edu.cn](mailto:minliu@csu.edu.cn)

Single-atom Fe-N-C catalysts are considered a candidate to replace the platinum group metals in oxygen reduction reaction (ORR), due to its high activity, anti-toxicity, and metal atom utilization<sup>1–4</sup>. Advanced Fe-N-C materials show comparable ORR performance to that of benchmark Pt/C<sup>3,5–7</sup>. Both theoretical and experimental studies indicate that the Fe-N<sub>4</sub> site is the active species of Fe-N-C catalysts<sup>3,4,6,8–10</sup>. However, the ORR activity of Fe-N<sub>4</sub> site on different carbon supports varies greatly, and Fe-N<sub>4</sub> ORR activity on curved carbon supports is usually orientation-dependence<sup>11–15</sup>. The essential of the difference and orientation-dependence of Fe-N<sub>4</sub> ORR activity remains unclear. Therefore, understanding the ORR activity of the Fe-N<sub>4</sub> site is crucial to further improve the ORR performance of Fe-N-C catalysts.

The intrinsic ORR activity of the Fe-N<sub>4</sub> site relates to the electronic structure of carbon supports<sup>7,16</sup>. Controlling the electronic structure of carbon supports alters the interaction between the supports and the Fe-N<sub>4</sub> site, resulting in the activity change of the Fe-N<sub>4</sub> site<sup>6,7,13,16–18</sup>. However, the essential of the change in Fe-N<sub>4</sub> ORR activity is still puzzling due to the complex factors affecting it. Some works reported that the electronic structure of carbon supports (electron-withdrawing/donating property) can affect the d-band center or d-orbital level of Fe site<sup>17,19–21</sup>. While, others claimed that it regulates the charge state of Fe site<sup>6,22,23</sup>. To understand the Fe-N<sub>4</sub> ORR activity, many efforts have been made to explore the descriptors of Fe-N<sub>4</sub> ORR activity<sup>13,16,20,24–26</sup>. For example, the full width at half-maximum of C 1s photoemission spectra<sup>13</sup>, d-band center<sup>20</sup>, and the electronegativity of the nearest neighbor atoms<sup>24</sup>, are considered to describe the ORR activity of the Fe-N<sub>4</sub> site. However, these descriptors are difficult to understand the orientation-dependence and differences of ORR activity at the same Fe-N<sub>4</sub> site on different carbon supports<sup>11,12,14</sup>. Therefore, elucidating the origin of ORR activity and exploring the universal descriptors of ORR activity on the Fe-N<sub>4</sub> site are urgent.

In this work, we demonstrate that the hybridization among Fe 3d<sub>z<sup>2</sup></sub>, 3d<sub>yz</sub> (3d<sub>xz</sub>), and O<sub>2</sub> π\* orbital is the origin of ORR activity on the Fe-N<sub>4</sub> site by density functional theory (DFT) calculations. We established the relationship between the geometric, electronic structure, and ORR activity of the Fe-N<sub>4</sub> site. From the geometric structure, the Fe–O bond length (L<sub>Fe–O</sub>) can accurately describe the ORR activity of the Fe-N<sub>4</sub> site. From the electronic structure, the d-band center gap of spin states (Δd), the magnetic moment of the Fe site (M<sub>Fe</sub>), and \*O<sub>2</sub> (M<sub>\*O<sub>2</sub></sub>) are nearly linear in relationship to the ORR activity of the Fe-N<sub>4</sub> site. We found that these descriptors and Fe-N<sub>4</sub> ORR activity are located in two regions. We provided a model to elucidate the origin and correlation of these descriptors from the spatial structure and level of the frontier orbital. This model reveals that descriptors essentially reflect hybridization between Fe 3d<sub>z<sup>2</sup></sub>, 3d<sub>yz</sub> (3d<sub>xz</sub>), and O<sub>2</sub> π\* orbital, which is related to the height of 3d orbital spatial distribution. This study offers new insights into the origin and descriptor of ORR activity on M-N-C catalysts and provides guidance for the design of high-performance ORR catalysts.

## Results

**Structural stability and ORR activity of Fe-N<sub>4</sub> sites.** Here, we build the model of the Fe-N<sub>4</sub> site embedded in the graphene slab (Fig. 1a). We introduced various divacancy defects around the Fe-N<sub>4</sub> site to obtain the various sample of Fe-N<sub>4</sub> ORR activity, since divacancy defects can modify the electronic structure of the carbon supports and also affect the ORR activity of the Fe-N<sub>4</sub> site<sup>13,16,22,27–29</sup>. Then pentagon-octagon-pentagon (5-8-5) defects were constructed by selectively removing C–C bonds around the Fe-N<sub>4</sub> site. Triple pentagon-triple heptagon (555-777) and pentagon-heptagon-heptagon-pentagon (5-7-7-5) defects

were obtained by rotating the different C–C bonds (Fig. 1b). A total of 42 types of divacancy defects were constructed around the Fe-N<sub>4</sub> site, including ten types of 5-8-5 (Supplementary Fig. 1), nine types of 555-777 (Supplementary Fig. 2), and 23 types of 5-7-7-5 (Supplementary Fig. 3) defects.

To evaluate the stability of single-atom Fe sites on carbon supports, we calculated the binding energy (E<sub>bind</sub>) of single-atom Fe sites (Fig. 1c). For the perfect Fe-N<sub>4</sub> configuration, the binding energy of the single-atom Fe site is –1.01 eV, indicating that the configuration of the Fe-N<sub>4</sub> site on carbon supports is stable. Under the control of divacancy defects, the binding energies of Fe sites range from –1.88 ~0.63 eV. Obviously, divacancy defects on the carbon supports can affect the stability of a single-atom Fe site. Among them, the relatively stable systems (E<sub>bind</sub> < –1.01 eV) were selected as examples to study the ORR activity of Fe-N<sub>4</sub> sites, which include 5-8-5 (6, 8, 9), 555-777 (5a, 6a, 7b, 8a, 9a), and 5-7-7-5 defect (6I, 7I, 8I, 8II, 8III, 9I, 10I). The ORR activity on the upper (blue) and lower (red) sides of Fe-N<sub>4</sub> configurations were investigated due to surface asymmetry (Fig. 1d). We found the hydrogenation of \*O<sub>2</sub> is a potential-determining step (PDS) at all Fe-N<sub>4</sub> configurations. Divacancy defect can regulate the free energy difference of this step on the Fe-N<sub>4</sub> site (Supplementary Table 1). The maximal free energy difference (ΔG<sub>max</sub>) of ORR at the perfect FeN<sub>4</sub> site is –0.45 eV, which is consistent with previous studies<sup>3,6,30</sup>. Among them, divacancy defects, such as 6, 5a, 6a, 6I, 7I, and 8I, can enhance the activity of the Fe-N<sub>4</sub> site, with ΔG<sub>max</sub> less than –0.60 eV (Fig. 1d). For the asymmetric surfaces, the ORR activity of the Fe-N<sub>4</sub> site showed orientation-dependence and difference, such as 6I, 7I, 8I, etc. Besides, divacancy defects can control the electron-donating capability of the carbon support, ultimately affecting the charge state and the d-band center of the Fe site (Supplementary Fig. 4). However, these factors are difficult to elucidate the orientation-dependence of the ORR activity of the Fe-N<sub>4</sub> site on an asymmetric surface.

**Factors of ORR activity at the Fe-N<sub>4</sub> site.** We investigated the ORR process of Fe-N<sub>4</sub> configurations from energy, geometry, and electronic structure to explore the origin of Fe-N<sub>4</sub> ORR activity. Here, we highlight the results of 6 (5-8-5), 6a (555-777), and 6I (5-7-7-5) models because they can improve the ORR activity of the Fe-N<sub>4</sub> site with good thermodynamic stability (Supplementary Fig. 5). The free energy diagram of ORR shows that the ΔG value of \*OOH formation on 6, 6a, and 6I are –0.62, –0.65, and –0.66 eV (Fig. 2a and Supplementary Fig. 6), respectively. Compared with the perfect FeN<sub>4</sub> site (–0.45 eV), divacancy defects (6, 6a, and 6I) can facilitate \*O<sub>2</sub> conversion to \*OOH intermediate. We found that the adsorption energy of \*O<sub>2</sub> with end-on1 and end-on2 configurations on the FeN<sub>4</sub> site are –0.53 and –0.41 eV, respectively, and the adsorption energy of \*O<sub>2</sub> with side-on configuration on the FeN<sub>4</sub> site is –0.01 eV (Supplementary Fig. 7). This result shows that the end-on adsorption is more favorable than the side-on adsorption at the FeN<sub>4</sub> site. Among them, the adsorption energies of \*O<sub>2</sub> on 6, 6a, and 6I are –0.34, –0.33, and –0.38 eV (Fig. 2b), respectively, which are larger than that of the perfect FeN<sub>4</sub> site (–0.53 eV). These results suggest the weak adsorption of \*O<sub>2</sub> on the Fe-N<sub>4</sub> site is the key to enhance the ORR activity of the Fe-N<sub>4</sub> site. Meanwhile, the O–O bond lengths on the O<sub>2</sub>@FeN<sub>4</sub>, O<sub>2</sub>@6, O<sub>2</sub>@6a, and O<sub>2</sub>@6I are 1.284, 1.297, 1.294, and 1.296 Å (Fig. 2b), respectively, which are longer than the bond length of O<sub>2</sub> molecule (1.234 Å). Besides, the Fe–O bond lengths on the O<sub>2</sub>@FeN<sub>4</sub>, O<sub>2</sub>@6, O<sub>2</sub>@6a, and O<sub>2</sub>@6I are 1.974, 1.745, 1.724, and 1.731 Å (Fig. 2b), respectively. These results reveal that divacancy defects (6, 6a, and 6I) can enhance the interaction between \*O<sub>2</sub> and Fe site and promote the activation of \*O<sub>2</sub>, thus increasing the Fe-N<sub>4</sub> ORR activity.

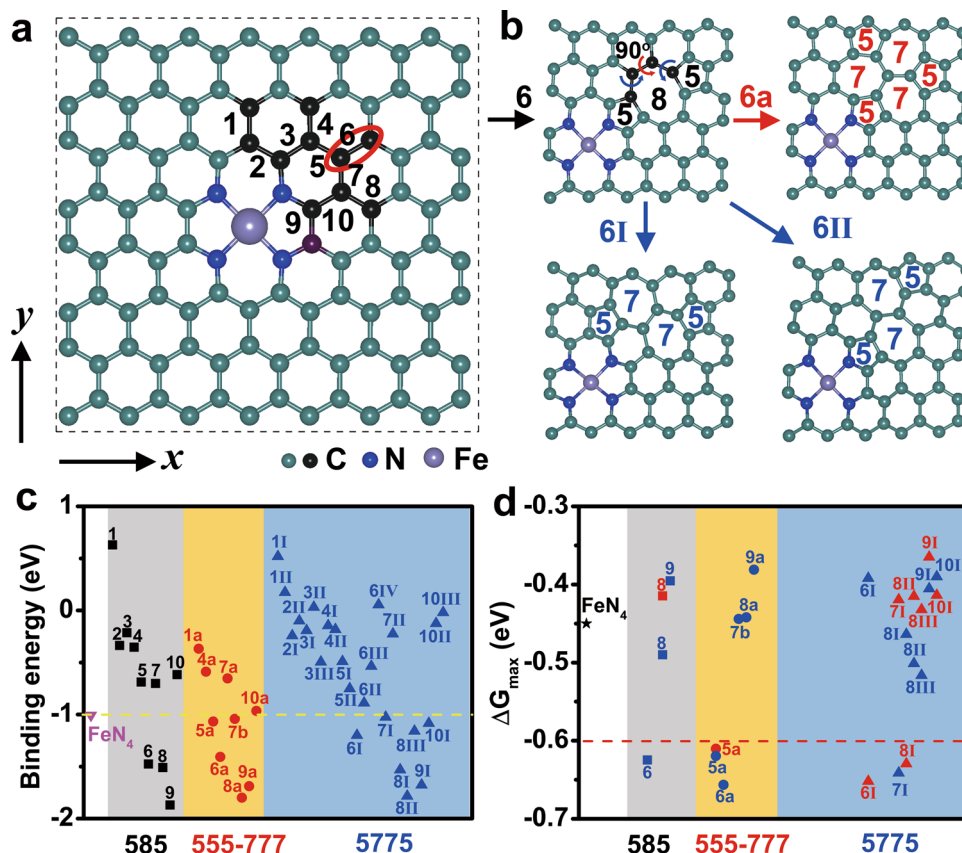


**Fig. 1 Modeling and performance evaluation of single-atom Fe-N<sub>4</sub> sites.** **a** Optimized structure of a perfect FeN<sub>4</sub> site. **b** Divacancy defect models 6, 6a, 6I, and 6II. **c** The binding energy of Fe site. **d** The ORR activity of Fe-N<sub>4</sub> sites. Blue and red represent upper and lower surface activity, respectively.

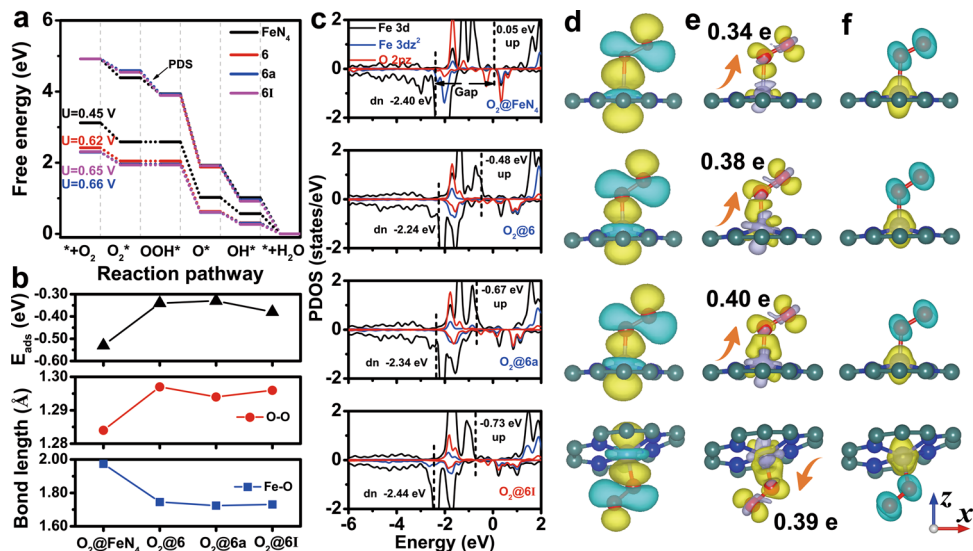


**Fig. 2 Theoretically study of the origin of Fe-N<sub>4</sub> ORR activity.** **a** Gibbs free energy diagrams of ORR on perfect FeN<sub>4</sub> site, 6, 6a, and 6I. **b** Adsorption energy of \*O<sub>2</sub>, O-O, and Fe-O bond length on the O<sub>2</sub>@FeN<sub>4</sub>, O<sub>2</sub>@6, O<sub>2</sub>@6a, and O<sub>2</sub>@6I. **c** Projected density of states of Fe 3d<sup>2</sup>, O<sub>2</sub> 2p<sub>z</sub> orbital, and d-band center of Fe 3d spin state. **d** Maximally localized Wannier functions of Fe 3d<sup>2</sup>, O<sub>2</sub> 2p<sub>z</sub> orbital. **e** Charge density difference and **f** spin density.

We studied the electronic structure of the Fe-N<sub>4</sub> site and O<sub>2</sub> to understand the activation mechanism of \*O<sub>2</sub>. Before the adsorption of O<sub>2</sub>, the projected density of state (PDOS) of the Fe site indicates that the Fe site has spin polarization with a spin magnetic moment of 2 μB. The occupied states of the Fe site near the Fermi level consist of localized 3dxz, 3dx<sup>2</sup>-y<sup>2</sup>, and 3dz<sup>2</sup> (Supplementary Fig. 8). Compared to the PDOS of the FeN<sub>4</sub> site,

divacancy defects (6, 6a, and 6I) modified the intensity and distribution of Fe 3d states (especially 3dxz and 3dz<sup>2</sup>). For the O<sub>2</sub> molecule, the PDOS of O<sub>2</sub> also shows spin polarization with a spin magnetic moment of 2 μB. The anti-bonding orbitals (π\*) of O<sub>2</sub> are mainly composed of the O<sub>2</sub> 2p<sub>y</sub> and 2p<sub>z</sub> orbitals (Supplementary Fig. 8). When O<sub>2</sub> adsorb on the Fe-N<sub>4</sub> site, the 2p<sub>z</sub> orbital in the O<sub>2</sub> π\* orbital split into the discrete level, and the

intensity of localized Fe  $3dz^2$  states is significantly reduced (Supplementary Fig. 9). A new hybrid state formed near the Fermi level, due to the hybridization between O<sub>2</sub>  $2pz$  and Fe  $3dz^2$  orbital. In the O<sub>2</sub>@6, O<sub>2</sub>@6a, and O<sub>2</sub>@6I, the strong hybridization between Fe  $3dz^2$ , and O  $2pz$  orbital lead to the significant discrete of the O<sub>2</sub>  $2pz$  orbital state (Fig. 2c), suggesting that the O<sub>2</sub> molecules are better activated. Besides, there is also hybridization between the  $2py$  orbital of O<sub>2</sub> and the  $3dyz$  orbital of Fe (Supplementary Fig. 9). The d-band center of Fe spin-up and spin-down are close to each other due to hybridization (Fig. 2c and Supplementary Fig. 4). The d-band center gap of Fe spin state ( $\Delta d$ ) of O<sub>2</sub>@FeN<sub>4</sub>, O<sub>2</sub>@6, O<sub>2</sub>@6a, and O<sub>2</sub>@6I are 2.45, 1.76, 1.67, and 1.70 eV (Fig. 2c), respectively, meaning the  $\Delta d$  is related to the activation of O<sub>2</sub>.

We also investigated the spatial distribution of Fe  $3dz^2$  ( $3dyz$ ) and O<sub>2</sub>  $2pz$  ( $2py$ ) orbital by the maximally localized Wannier functions (MLWF)<sup>31</sup>. The Wannier function of Fe  $3dz^2$  and Fe  $3dyz$  are located vertically and slant (Supplementary Figs. 10 and 11). O<sub>2</sub>  $2pz$  orbital Wannier function shows high mirror symmetry (Supplementary Fig. 12). When O<sub>2</sub> is adsorbed on the Fe-N<sub>4</sub> site, the Wannier function of Fe  $3dz^2$  ( $3dyz$ ) and O<sub>2</sub>  $2pz$  ( $2py$ ) shows the trend of orbital matching (Fig. 2d and Supplementary Figs. 13, 14). Wannier function of Fe  $3dz^2$  orbital decreases with that of O<sub>2</sub>  $2pz$  orbital increases (Fig. 2d and Supplementary Fig. 13). Especially, the changes of Fe  $3dz^2$  ( $3dyz$ ) and O<sub>2</sub>  $2pz$  ( $2py$ ) orbital Wannier functions on O<sub>2</sub>@6, O<sub>2</sub>@6a, and O<sub>2</sub>@6I are larger than that on O<sub>2</sub>@FeN<sub>4</sub>. These results demonstrate that divacancy defects (6, 6a, and 6I) can enhance the hybridization between Fe and O<sub>2</sub> to facilitate the activation of O<sub>2</sub>.

Generally, the filling of electrons in the O<sub>2</sub>  $\pi^*$  orbital is the beginning of the activation of O<sub>2</sub>. Charge density difference and Bader charge analysis reveal \*O<sub>2</sub> gain 0.34, 0.38, 0.40, and 0.39  $e$  from perfect FeN<sub>4</sub>, 6, 6a, and 6I (Fig. 2e), respectively. The electron-gaining region (yellow region) of the \*O<sub>2</sub> mainly distributes in the  $\pi^*$  orbitals of O<sub>2</sub>, which is consistent with the distribution region of the Wannier function (Fig. 2d and Supplementary Figs. 13, 14), reflecting that the electron transfer between Fe  $3dz^2$  ( $3dyz$ ) and O<sub>2</sub>  $\pi^*$  orbitals. Furthermore, due to electrons transfer between Fe sites and O<sub>2</sub>, the Fe  $3dz^2$  ( $3dyz$ ) and O<sub>2</sub>  $\pi^*$  orbitals are broken, thus changing the magnetic moment of the Fe site and O<sub>2</sub>. Spin density analysis show divacancy defects (6, 6a, and 6I) hardly change the spin density of Fe sites before O<sub>2</sub> adsorption (Supplementary Fig. 15). After O<sub>2</sub> adsorption, the spin density is mainly localized at the Fe site and \*O<sub>2</sub> has the opposite direction (Fig. 2f). The spin density of the Fe site and \*O<sub>2</sub> in the O<sub>2</sub>@6, O<sub>2</sub>@6a, and O<sub>2</sub>@6I is weaker than that in O<sub>2</sub>@FeN<sub>4</sub> (Fig. 2f). Therefore, the origin of O<sub>2</sub> activation is the hybridization of the Fe  $3dz^2$  ( $3dyz$ ) and \*O<sub>2</sub>  $2pz$  ( $2py$ ) orbitals, which results in electron transfer from the Fe site to \*O<sub>2</sub>, breaking the Fe  $3dz^2$  ( $3dyz$ ) and O<sub>2</sub>  $2pz$  ( $2py$ ) orbitals and reducing  $\Delta d$  and magnetic moments.

**Descriptors of ORR activity at Fe-N<sub>4</sub> sites.** As mentioned above, the adsorption energy of \*O<sub>2</sub>, the bond length, the charge state,  $\Delta d$ , and the magnetic moment may be related to the ORR activity of the Fe-N<sub>4</sub> site (Supplementary Table 2). To gain accurate descriptors for the ORR activity of the Fe-N<sub>4</sub> site, we investigated the correlation between these factors and ORR activity (Fig. 3 and Supplementary Figs. 16–18). According to the free energy diagram, the adsorption energy of \*O<sub>2</sub> may be related to ORR activity. The adsorption energy of \*O<sub>2</sub> at the Fe-N<sub>4</sub> site ranges from -0.6 to -0.1 eV under the regulation of divacancy defects (Supplementary Fig. 16). The linear fitting results reveal that the coefficient of determination R-square between the adsorption energy of \*O<sub>2</sub> and the ORR activity of the Fe-N<sub>4</sub> site is 0.15. No

direct correlation between the adsorption energy of \*O<sub>2</sub> and ORR activity at the Fe-N<sub>4</sub> site. From the geometric structure, the O–O bond length ( $L_{O-O}$ ) is related to the activation of O<sub>2</sub> molecules, and the Fe–O bond length ( $L_{Fe-O}$ ) can reveal the strength of the interaction between \*O<sub>2</sub> and Fe-N<sub>4</sub> site. Herein, we found that the O–O bond length is distributed between 1.264–1.298 Å by regulating divacancy defects (Supplementary Fig. 17). When the O–O bond length is larger than 1.290 Å, and the free energy difference for hydrogenation of \*O<sub>2</sub> is less than -0.6 eV. The coefficient of determination R-square between the O–O bond length and Fe-N<sub>4</sub> ORR activity is 0.81, with the relevant formula being  $\Delta G = -9.93L_{O-O} + 12.3$  (Supplementary Fig. 17). Besides, the length of the Fe–O bond is distributed in stages (Fig. 3a). For the active Fe-N<sub>4</sub> site (golden circle), the average Fe–O bond length is around 1.737 Å. For the inactive Fe-N<sub>4</sub> site (blue circle), the average Fe–O bond length is near 2.013 Å. The coefficient of determination R-square between the Fe–O bond length and Fe-N<sub>4</sub> ORR activity is 0.95 (Fig. 3a), indicating the Fe–O bond length can accurately describe the ORR activity of the Fe-N<sub>4</sub> site with the relevant formula  $\Delta G = 0.75L_{Fe-O} + 1.94$ .

From the electronic structure, the charge state of the Fe site (\*O<sub>2</sub>) can reflect the electrons transfer between Fe and O<sub>2</sub>, which may have a potential relationship with Fe-N<sub>4</sub> ORR activity (Supplementary Fig. 18). The Bader charge state of Fe and \*O<sub>2</sub> are -1.22 to -1.13  $e$  and 0.24 to 0.41  $e$  (Supplementary Fig. 18), respectively, due to the regulation of divacancy defect. The linear fitting results show that the coefficient of determination R-square between the charge state of the Fe site (\*O<sub>2</sub>) and the ORR activity of the Fe-N<sub>4</sub> site is 0.10 (0.58), indicating that they are difficult to describe the ORR activity of Fe-N<sub>4</sub> site (Supplementary Fig. 18). In addition,  $\Delta d$  (Fig. 3b),  $M_{Fe}$  (Fig. 3c), and  $M_{*O_2}$  (Fig. 3d) are also characteristic symbols for the change of Fe and \*O<sub>2</sub> electronic structure. We found that  $\Delta d$ ,  $M_{Fe}$ , and  $M_{*O_2}$  are also distributed in stages (Fig. 3b–d). The smaller their values, the higher the ORR activity of the Fe-N<sub>4</sub> site. After the adsorption of O<sub>2</sub>, the average values of  $\Delta d$ ,  $M_{Fe}$ , and  $M_{*O_2}$  on the active Fe-N<sub>4</sub> site (golden circle) are 1.755 eV, 1.190  $\mu B$ , and 0.881  $\mu B$ , respectively. Correspondingly, the average of  $\Delta G$  is -0.638 eV. For the inactive Fe-N<sub>4</sub> sites (blue circle), the average of  $\Delta G$ ,  $\Delta d$ ,  $M_{Fe}$ , and  $M_{*O_2}$  are -0.430 eV, 2.570 eV, 1.756  $\mu B$ , and 1.177  $\mu B$ , respectively. These fitting results show that the correlation between  $\Delta d$ ,  $M_{Fe}$ ,  $M_{*O_2}$ , and  $\Delta G$  is nearly linear. The R-squares are 0.95, 0.94, and 0.91 (Fig. 3b–d), respectively, indicating  $\Delta d$ ,  $M_{Fe}$ ,  $M_{*O_2}$  are promising ORR activity descriptors for the Fe-N<sub>4</sub> site. The relevant formulas are  $\Delta G = 0.25\Delta d - 1.08$ ,  $\Delta G = 0.37M_{Fe} - 1.08$ ,  $\Delta G = 0.67M_{*O_2} - 1.22$ , respectively.

To generalize the correlations between electronic structure and Fe-N<sub>4</sub> ORR activity, we calculated the electronic structure of O<sub>2</sub>@Fe-N<sub>4</sub> by using other theoretical approximations, including local density approximation (LDA (CA))<sup>32,33</sup>, Perdew–Wang 91 (GGA (PW91))<sup>34</sup>, strongly constrained and appropriately normed semilocal density functional (meta-GGA (SCAN))<sup>35</sup>, and Heyd–Scuseria–Ernzerhof screened hybrid density functional (HSE06)<sup>36,37</sup>. The results show that the type of DFT exchange–correlation functional can affect the absolute value of the spin magnetic moment of Fe ( $M_{Fe}$ ), the spin magnetic moment of \*O<sub>2</sub> ( $M_{*O_2}$ ), and the d-band center gap of spin state ( $\Delta d$ ), but the variation tendency of the value is consistent (Supplementary Figs. 19–22 and Supplementary Tables 3–5). There is still a nearly linear correlation between electronic structure and Fe-N<sub>4</sub> ORR activity in the theoretical framework of LDA (CA) + U, GGA (PW91) + U, meta-GGA (SCAN), and HSE06 (Supplementary Figs. 20–22).  $M_{Fe}$ ,  $M_{*O_2}$ , and  $\Delta d$  are still distributed in stages. For the LDA (CA) + U, GGA (PW91) + U, meta-GGA (SCAN), and HSE06, the R-Square between  $M_{Fe}$  and  $\Delta G$  are 0.93, 0.95, 0.91, and 0.91



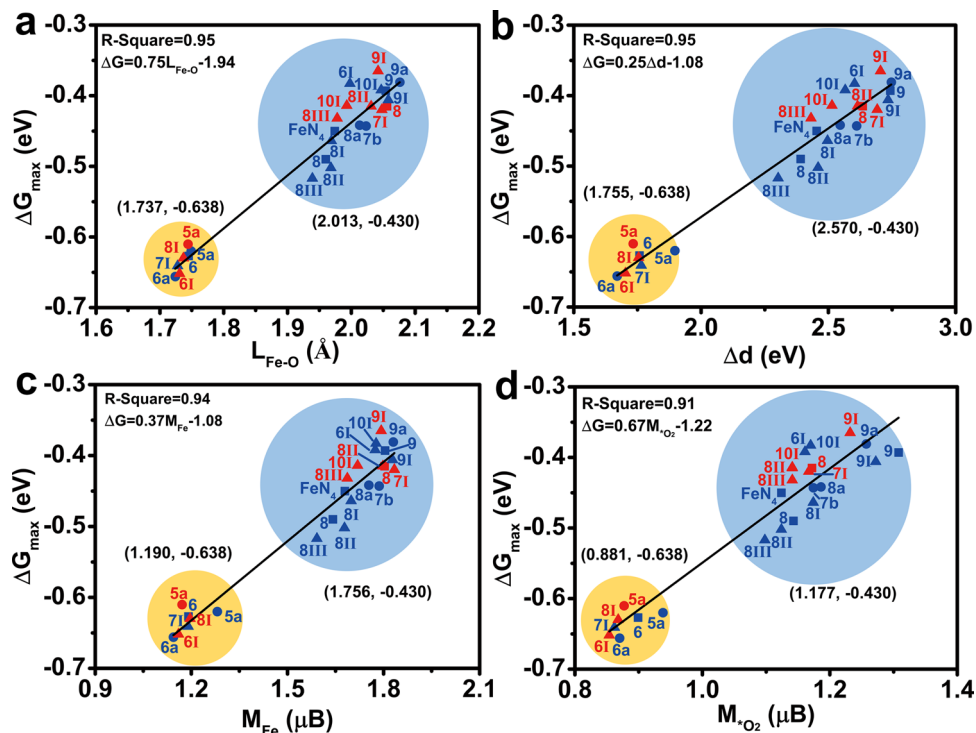


**Fig. 3 Exploring the descriptors of Fe-N<sub>4</sub> ORR activity.** Correlation between the **a**  $L_{\text{Fe-O}}$  (Fe-O bond length), **b**  $\Delta d$  (the d-band center gap of Fe spin state), **c**  $M_{\text{Fe}}$  (the spin magnetic moment of Fe), **d**  $M_{*O_2}$  (the spin magnetic moment of  $*O_2$ ) and the ORR activity of Fe-N<sub>4</sub> site. Blue and red represent upper and lower surface activity, respectively. Golden and blue circles represent the active and inactive Fe-N<sub>4</sub> site, respectively.

(Supplementary Fig. 20), respectively. In addition,  $M_{*O_2}$  and  $\Delta d$  were also highly correlated with  $\Delta G$  (Supplementary Figs. 21 and 22). Therefore, the correlation between the electronic structure and the Fe-N<sub>4</sub> ORR activity remains valid in other theoretical approximations.

**Correlations between the descriptors of ORR activity at Fe-N<sub>4</sub> sites.** We explored the correlation between these descriptors. Obviously, there is a nearly linear relationship between  $\Delta d$ ,  $M_{\text{Fe}}$ ,  $M_{*O_2}$ , and the Fe-O bond length, with the R-squares of 0.98, 0.99, and 0.94 (Fig. 4a and Supplementary Fig. 23), respectively, indicating that these descriptors can reflect the origin of Fe-N<sub>4</sub> ORR activity. To reveal the essence of descriptors, we analyzed the projected magnetic moment of Fe, the spatial structure of Fe 3d and O<sub>2</sub>  $\pi^*$  orbital, and the schematic frontier orbital level diagram.

The projected magnetic moment of Fe fluctuates obviously, due to the regulation of the divacancy defects (Fig. 4b). Only when the magnetic moments of  $3dz^2$  and  $3dyz + 3dxz$  decrease at the same time, the Fe-N<sub>4</sub> site shows higher ORR activity. This result suggests that the ORR activity at the active Fe-N<sub>4</sub> site is attributed to the strong hybridization of Fe  $3dz^2$ - $*O_2$  2p<sub>z</sub> and Fe  $3dyz$ - $*O_2$  2p<sub>y</sub> (Fe  $3dxz$ - $*O_2$  2p<sub>x</sub>).

The spatial distribution of Fe 3d and O<sub>2</sub>  $\pi^*$  orbital can elucidate the correlation between the Fe-O bond length and  $M_{\text{Fe}}$ . As shown in Fig. 4c, the  $3dxy$  ( $3dx^2-y^2$ ),  $3dyz$  ( $3dxz$ ) and  $3dz^2$  are different heights in the Z direction. When the Fe-O bond is long, the activation of O<sub>2</sub> attribute to the hybridization between Fe  $3dz^2$  and O<sub>2</sub> 2p<sub>z</sub> orbital, which leads to the decrease of the projected magnetic moments of Fe  $3dz^2$ . When the Fe-O bond is short, the activation of O<sub>2</sub> is additionally improved by the hybridization of Fe  $3dyz$  ( $3dxz$ ) and 2p<sub>y</sub> (2p<sub>x</sub>) orbitals. Meanwhile, the projected magnetic moments of Fe  $3dz^2$  and  $3dyz$  ( $3dxz$ ) are significantly reduced. The Fe  $3dxy$  and  $3dx^2-y^2$  have weak hybridization with O<sub>2</sub>  $\pi^*$  orbital due to their low

spatial distribution in the Z direction. Thereby the projected magnetic moments of  $3dxy$  and  $3dx^2-y^2$  vary only slightly.

The schematic frontier orbital diagram of O<sub>2</sub>@Fe-N<sub>4</sub> can reveal the differences in O<sub>2</sub> activation (Fig. 4d)<sup>38</sup>. Before the adsorption of O<sub>2</sub>, the Fe 3d orbital splits into an empty  $3dxy$ , singly occupied  $3dyz$ ,  $3dz^2$  type orbitals, and occupied  $3dxz$ ,  $3dx^2-y^2$  orbitals, due to Fe 3d orbital hybridization with the carbon support. For the O<sub>2</sub>@Fe-N<sub>4</sub>, the differences in O<sub>2</sub> activation is attributed to the degree of hybridization of Fe  $3dz^2$  and  $3dyz$  (or  $3dxz$ ) with O<sub>2</sub>  $\pi^*$  orbital. For the active Fe-N<sub>4</sub> site, the strong hybridization of  $3dz^2$  and  $3dyz$  (or  $3dxz$ ) with O<sub>2</sub>  $\pi^*$  orbital promote the O<sub>2</sub> activation. For the inactive Fe-N<sub>4</sub> site, the strong hybridization of  $3dz^2$  with O<sub>2</sub>  $\pi^*$  orbital and negligible hybridization of  $3dyz$  (or  $3dxz$ ) with O<sub>2</sub>  $\pi^*$  orbital lead to the poor O<sub>2</sub> activation. The change of  $\Delta d$ ,  $M_{\text{Fe}}$ , and  $M_{*O_2}$  are also due to the above factors. Therefore, the Fe-N<sub>4</sub> ORR activity is origin from the activation of O<sub>2</sub>, that is, the hybridization between Fe  $3dz^2$  ( $3dyz$  or  $3dxz$ ) and  $*O_2$   $\pi^*$  orbital. The Fe-O bond length,  $\Delta d$ ,  $M_{\text{Fe}}$ , and  $M_{*O_2}$  are the specific symbols describing hybridization.

## Discussion

In this work, we investigated the origin and descriptors of ORR activity on the Fe-N<sub>4</sub> site using DFT calculation. We explored divacancy defects on carbon supports that could modulate the ORR activity of the Fe-N<sub>4</sub> site. The first electron step ( $*O_2 + H^+ + e \rightarrow *OOH$ ) is the potential-determining step (PDS) on all Fe-N<sub>4</sub> configurations. Fe-N<sub>4</sub> site on 6, 5a, 6a, 6l, 7l, and 8l showed high ORR activity with  $\Delta G_{\text{max}}$  less than -0.60 eV. The ORR activity of Fe-N<sub>4</sub> sites on the asymmetric surface showed orientation-dependence. We demonstrated that the hybridization between Fe  $3dz^2$ ,  $3dyz$  ( $3dxz$ ), and O<sub>2</sub>  $\pi^*$  orbitals is the origin of Fe-N<sub>4</sub> ORR activity by studying the electronic structure. The Fe-O bond length,  $\Delta d$ ,  $M_{\text{Fe}}$ , and  $M_{*O_2}$  show staged differences, which can be used as descriptors to accurately describe the ORR activity of the

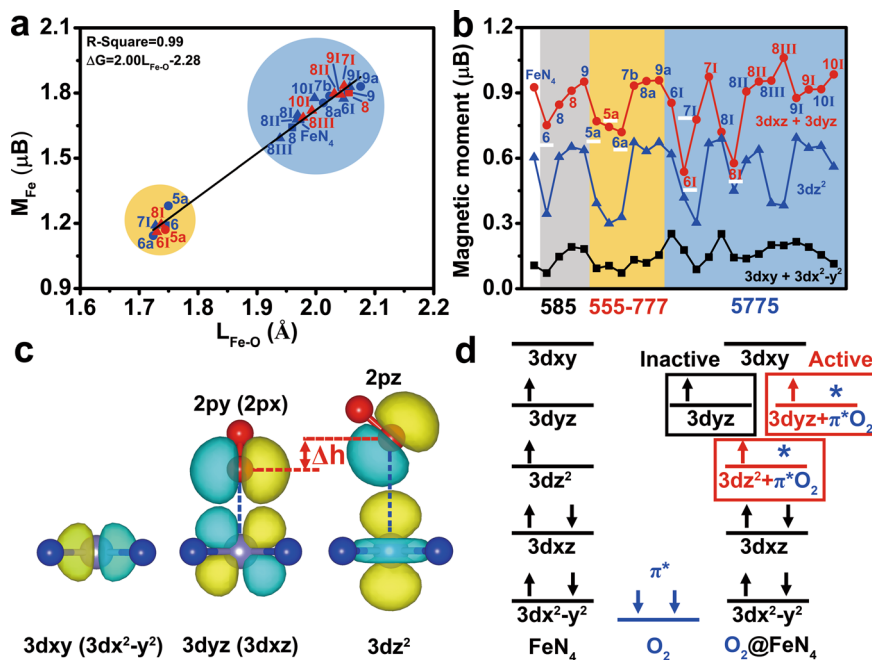


**Fig. 4 Correlation mechanisms between descriptors.** **a** Correlation between the Fe–O bond length and magnetic moment of Fe site. **b** The magnetic moment of the  $3dx_y + 3dx^2 - y^2$ ,  $3d_{yz} + 3dx_z$  and  $3dz^2$  orbital at the Fe site. **c** The spatial distribution of Fe  $3d_{xy}$  ( $3dx^2 - y^2$ ),  $3d_{yz}$  ( $3dx_z$ ),  $3dz^2$ , and  $O_2$   $2\pi^*$  orbital. **d** The schematic frontier orbital diagram of  $Fe-N_4$ ,  $O_2$ , and  $O_2@Fe-N_4$ .

$Fe-N_4$  site. There is a nearly linear correlation between  $\Delta d$ ,  $M_{Fe}$ ,  $M_{*O_2}$ , and the Fe–O bond length from geometry and electron structure. Importantly, we elucidate that the Fe–O bond length,  $\Delta d$ ,  $M_{Fe}$ , and  $M_{*O_2}$  are essentially hybrids between Fe  $3dz^2$  ( $3d_{yz}$ ) and  $O_2$   $\pi^*$  orbitals from the spatial distribution and energy level of the frontier orbital. The height of the Fe  $3d$  projected orbital is related to the activation of  $O_2$ . For the active  $Fe-N_4$  sites, the strong hybridization of  $3dz^2$  and  $3d_{yz}$  (or  $3dx_z$ ) with  $O_2$   $\pi^*$  orbital results in the short Fe–O bond length (1.737 Å), low  $\Delta d$  (1.755 eV),  $M_{Fe}$  (1.190  $\mu_B$ ), and  $M_{*O_2}$  (0.881  $\mu_B$ ). For the inactive  $Fe-N_4$  site, the strong hybridization of  $3dz^2$  with  $O_2$   $\pi^*$  orbital and the negligible hybridization of  $3d_{yz}$  ( $3dx_z$ ) with  $O_2$   $\pi^*$  orbital lead to the long Fe–O bond length (2.013 Å), high  $\Delta d$  (2.570 eV),  $M_{Fe}$  (1.756  $\mu_B$ ), and  $M_{*O_2}$  (1.177  $\mu_B$ ). This work offers insights into the  $Fe-N_4$  ORR activity and provides guidelines for designing the high-performance Fe–N–C catalysts.

## Methods

**DFT calculations.** Our spin-polarized density functional theory simulation was calculated by using the Vienna ab initio simulation package (VASP)<sup>39</sup>. The PAW potentials and the generalized gradient approximation (GGA) of Perdew–Burke–Ernzerhof (PBE) were employed to describe the interaction of electron-ion and the electron–electron exchange and correlation functional, respectively<sup>40,41</sup>. After the test, the cutoff energy was set at 400 eV, and Monkhorst–Pack mesh with a  $2 \times 2 \times 1$  grid was used in our calculations after testing (Supplementary Fig. 24). van der Waals (VDW) forces were corrected with the D2 method of Grimme<sup>42</sup>. The convergence criterion was set at  $0.02 \text{ eV } \text{\AA}^{-1}$  for the force and  $1 \times 10^{-5} \text{ eV}$  per atom for energy. We used the correlation energy (U) of 4 eV and the exchange energy (J) of 1 eV for Fe  $3d$  orbitals<sup>43,44</sup>. We built a super-cell ( $7 \times 8$ ) carbon substrate as a model, which includes 106 C atoms, 4 N atoms, and 1 Fe atom. The lattice parameters of this slab are  $a = 17.31 \text{ \AA}$  and  $b = 16.98 \text{ \AA}$  after optimization. The lattice constants are optimized again due to the introduction of divacancy defects in the system. The vacuum layer was set at 15 Å. Maximally localized Wannier functions (MLWFs) methods are applied by Wannier90 to calculate the spatial distribution of Fe  $3d$  and  $O_2$   $2p$  orbital<sup>31,45–47</sup>. We also considered the effect of solvent on the ORR activity of the  $Fe-N_4$  site by employing an implicit solvent model<sup>48,49</sup>. To confirm the generalization validity of the correlation between electronic structure and  $Fe-N_4$  ORR activity, local density approximation with the Ceperly–Alder functional (LDA (CA))<sup>32,33</sup>, Perdew–Wang 91 (GGA (PW91))<sup>34</sup>, strongly constrained and appropriately normed semilocal density functional (meta-GGA (SCAN))<sup>35</sup>, and Heyd–Scuseria–Ernzerhof screened hybrid density functional (HSE06) were used to evaluate the electronic

structure<sup>36,37</sup>. In the framework of LDA (CA) and GGA (PW91), we also consider the Coulomb interaction between Fe  $3d$  orbital electrons, and the Hubbard U value is 3 eV. First-principles Born–Oppenheimer molecular dynamics (BOMD) simulation was performed in the canonical ensemble with Nosé–Hoover heat bath schemes<sup>50,51</sup>. During the simulation, spin polarization is not considered, and the Brillouin-zone integrations were performed using the Gamma-point grid. The total simulation time is 5 ps with a time step of 1 fs at 300 K. We also used the VESTA package to visualize the structures and charge density differences<sup>52</sup>.

The binding energy of the Fe site ( $E_{bind}$ ) on the carbon supports can be calculated by

$$E_{bind} = E_{Fe@sub} - E_{sub} - E_{Fe-bulk} \quad (1)$$

where  $E_{Fe@sub}$  is the total energy of the Fe atom embedded in the carbon supports;  $E_{sub}$  and  $E_{Fe}$  are the energies of the substrate and single Fe atom in the Fe bulk, respectively.

The Gibbs free energy can be expressed as

$$\Delta G = \Delta E + \Delta ZPE - T \cdot \Delta S \quad (2)$$

where  $\Delta E$ ,  $\Delta ZPE$ , and  $\Delta S$  are the reaction energy calculated by the DFT methods, the changes in zero-point energies, and the entropy during the reaction, respectively<sup>53–55</sup>. T is the temperature (298.15 K, in our work).

The d-band center gap of spin state ( $\Delta d$ ) can be defined as

$$\Delta d = |\epsilon_{up} - \epsilon_{dn}| = \left| \frac{\int_{-\infty}^{+\infty} n_{up}(\epsilon) \epsilon d\epsilon}{\int_{-\infty}^{+\infty} n_{up}(\epsilon) d\epsilon} - \frac{\int_{-\infty}^{+\infty} n_{dn}(\epsilon) \epsilon d\epsilon}{\int_{-\infty}^{+\infty} n_{dn}(\epsilon) d\epsilon} \right| \quad (3)$$

where  $\epsilon_{up}$  is the d-band center of the Fe  $3d$  spin-up projected density of states. And  $\epsilon_{dn}$  is the d-band center of the Fe  $3d$  spin-down projected density of states<sup>56</sup>.

The magnetic moment (M) is defined as

$$M = N(\text{spin-up}) - N(\text{spin-down}) \quad (4)$$

$$M = M(3d_{xy}) + M(3dx^2 - y^2) + M(3d_{yz}) + M(3dx_z) + M(3dz^2) \quad (5)$$

where  $N(\text{spin-up})$  and  $N(\text{spin-down})$  represent the number of electrons in the spin-up and spin-down occupied state, respectively<sup>57,58</sup>.  $M(3d_{xy})$ ,  $M(3dx^2 - y^2)$ ,  $M(3d_{yz})$ ,  $M(3dx_z)$ , and  $M(3dz^2)$  represent the projected of magnetic moments on Fe  $3d_{xy}$ ,  $3dx^2 - y^2$ ,  $3d_{yz}$ ,  $3dx_z$ , and  $3dz^2$ , respectively.

## Data availability

The data that support the findings of this study are available from the corresponding author on reasonable request.

## Code availability

The computational codes used in this work are available from the corresponding author on reasonable request.

Received: 8 October 2021; Accepted: 31 March 2022;

Published online: 19 April 2022

## References

- Peng, H. et al. Effect of transition metals on the structure and performance of the doped carbon catalysts derived from polyaniline and melamine for ORR application. *ACS Catal.* **4**, 3797–3805 (2014).
- Han, J. et al. Single-atom Fe-N<sub>x</sub>-C As an efficient electrocatalyst for zinc-air batteries. *Adv. Funct. Mater.* **29**, 1808872 (2019).
- Jiang, R. et al. Edge-site engineering of atomically dispersed Fe-N<sub>4</sub> by selective C-N bond cleavage for enhanced oxygen reduction reaction activities. *J. Am. Chem. Soc.* **140**, 11594–11598 (2018).
- Li, J. et al. Identification of durable and non-durable Fe-N<sub>x</sub> sites in Fe-N-C materials for proton exchange membrane fuel cells. *Nat. Catal.* **4**, 10–19 (2020).
- Jiao, L. et al. Chemical vapour deposition of Fe-N-C oxygen reduction catalysts with full utilization of dense Fe-N<sub>4</sub> sites. *Nat. Mater.* **20**, 1385–1391 (2021).
- Lin, Y. et al. Tuning charge distribution of FeN<sub>4</sub> via external N for enhanced oxygen reduction reaction. *ACS Catal.* **11**, 6304–6315 (2021).
- Zhao, C. X., Li, B. Q., Liu, J. N. & Zhang, Q. Intrinsic electrocatalytic activity regulation of M-N-C single-atom catalysts for the oxygen reduction reaction. *Angew. Chem. Int. Ed.* **60**, 4448–4463 (2021).
- Zhang, H. et al. High-performance fuel cell cathodes exclusively containing atomically dispersed iron active sites. *Energy Environ. Sci.* **12**, 2548–2558 (2019).
- Li, J. et al. Structural and mechanistic basis for the high activity of Fe-N-C catalysts toward oxygen reduction. *Energy Environ. Sci.* **9**, 2418–2432 (2016).
- Marshall-Roth, T. et al. A pyridinic Fe-N<sub>4</sub> macrocycle models the active sites in Fe/N-doped carbon electrocatalysts. *Nat. Commun.* **11**, 5283 (2020).
- Li, J. et al. Thermally driven structure and performance evolution of atomically dispersed FeN<sub>4</sub> sites for oxygen reduction. *Angew. Chem. Int. Ed.* **58**, 18971–18980 (2019).
- Wu, Y. et al. Compressive strain modulation of single iron sites on helical carbon support boosts electrocatalytic oxygen reduction. *Angew. Chem. Int. Ed.* **60**, 22722–22728 (2021).
- Ramaswamy, N., Tylus, U., Jia, Q. & Mukerjee, S. Activity descriptor identification for oxygen reduction on nonprecious electrocatalysts: Linking surface science to coordination chemistry. *J. Am. Chem. Soc.* **135**, 15443–15449 (2013).
- Wang, Y. et al. CoN<sub>4</sub> active sites in locally distorted carbon structure for efficient oxygen reduction reaction via regulating coordination environment. *Chem. Eng. J.* **429**, 132119 (2022).
- Liu, D. et al. Atomically dispersed platinum supported on curved carbon supports for efficient electrocatalytic hydrogen evolution. *Nat. Energy* **4**, 512–518 (2019).
- Asset, T. & Atanassov, P. Iron-nitrogen-carbon catalysts for proton exchange membrane fuel cells. *Joule* **4**, 33–44 (2020).
- Mun, Y. et al. Versatile strategy for tuning ORR activity of a single Fe-N<sub>4</sub> site by controlling electron-withdrawing/donating properties of a carbon plane. *J. Am. Chem. Soc.* **141**, 6254–6262 (2019).
- Chen, Y. et al. Enhanced oxygen reduction with single-atomic-site iron catalysts for a zinc-air battery and hydrogen-air fuel cell. *Nat. Commun.* **9**, 5422 (2018).
- Zhang, J. et al. Tuning the coordination environment in single-atom catalysts to achieve highly efficient oxygen reduction reactions. *J. Am. Chem. Soc.* **141**, 20118–20126 (2019).
- Luo, G., Wang, Y. & Li, Y. Two-dimensional iron-porphyrin sheet as a promising catalyst for oxygen reduction reaction: A computational study. *Sci. Bull.* **62**, 1337–1343 (2017).
- Yang, G. et al. Regulating Fe-spin state by atomically dispersed Mn-N in Fe-N-C catalysts with high oxygen reduction activity. *Nat. Commun.* **12**, 1734 (2021).
- Wang, X. et al. Edge-rich Fe-N<sub>4</sub> active sites in defective carbon for oxygen reduction catalysis. *Adv. Mater.* **32**, e2000966 (2020).
- Zhang, N. et al. High-purity pyrrole-type FeN<sub>4</sub> sites as a superior oxygen reduction electrocatalyst. *Energy Environ. Sci.* **13**, 111–118 (2020).
- Xu, H., Cheng, D., Cao, D. & Zeng, X. C. A universal principle for a rational design of single-atom electrocatalysts. *Nat. Catal.* **1**, 339–348 (2018).
- Zagal, J. H. & Koper, M. T. Reactivity descriptors for the activity of molecular MN<sub>4</sub> catalysts for the oxygen reduction reaction. *Angew. Chem. Int. Ed.* **55**, 14510–14521 (2016).
- Zhong, W. et al. Electronic spin moment as a catalytic descriptor for Fe single-atom catalysts supported on C<sub>2</sub>N. *J. Am. Chem. Soc.* **143**, 4405–4413 (2021).
- Carr, L. D. & Lusk, M. T. Defect engineering: graphene gets designer defects. *Nat. Nanotechnol.* **5**, 316–317 (2010).
- Kim, Y., Ihm, J., Yoon, E. & Lee, G.-D. Dynamics and stability of divacancy defects in graphene. *Phys. Rev. B* **84**, 075445 (2011).
- Fu, X. et al. Tailoring FeN<sub>4</sub> sites with edge enrichment for boosted oxygen reduction performance in proton exchange membrane fuel cell. *Adv. Energy Mater.* **9**, 1803737 (2019).
- Chen, K. et al. Iron phthalocyanine with coordination induced electronic localization to boost oxygen reduction reaction. *Nat. Commun.* **11**, 4173 (2020).
- Fu, Z., Yang, B. & Wu, R. Understanding the activity of single-atom catalysis from frontier orbitals. *Phys. Rev. Lett.* **125**, 156001 (2020).
- Kohn, W. & Sham, L. J. Self-consistent equations including exchange and correlation effects. *Phys. Rev.* **140**, A1133–A1138 (1965).
- Ceperley, D. M. & Alder, B. J. Ground state of the electron gas by a stochastic method. *Phys. Rev. Lett.* **45**, 566–569 (1980).
- Perdew, J. P. & Wang, Y. Accurate and simple analytic representation of the electron-gas correlation energy. *Phys. Rev. B* **45**, 13244–13249 (1992).
- Sun, J., Ruzsinszky, A. & Perdew, J. P. Strongly constrained and appropriately normed semilocal density functional. *Phys. Rev. Lett.* **115**, 036402 (2015).
- Heyd, J., Scuseria, G. E. & Ernzerhof, M. Hybrid functionals based on a screened Coulomb potential. *J. Chem. Phys.* **118**, 8207–8215 (2003).
- Heyd, J., Scuseria, G. E. & Ernzerhof, M. Erratum: Hybrid functionals based on a screened Coulomb potential. *J. Chem. Phys.* **124**, 219906 (2006).
- Loipersberger, M., Cabral, D. G. A., Chu, D. B. K. & Head-Gordon, M. Mechanistic insights into Co and Fe quaterpyridine-based CO<sub>2</sub> reduction catalysts: metal-ligand orbital interaction as the key driving force for distinct pathways. *J. Am. Chem. Soc.* **143**, 744–763 (2021).
- Kresse, G. & Hafner, J. Ab initio molecular-dynamics simulation of the liquid-metal-amorphous-semiconductor transition in germanium. *Phys. Rev. B* **49**, 14251–14269 (1994).
- Bloch, P. E. Projector augmented-wave method. *Phys. Rev. B* **50**, 17953–17979 (1994).
- Perdew, J. P., Burke, K. & Ernzerhof, M. Generalized gradient approximation made simple. *Phys. Rev. Lett.* **77**, 3865–3868 (1996).
- Grimme, S. Semiempirical GGA-type density functional constructed with a long-range dispersion correction. *J. Comput. Chem.* **27**, 1787–1799 (2006).
- Wang, Y., Tang, Y. J. & Zhou, K. Self-adjusting activity induced by intrinsic reaction intermediate in Fe-N-C single-atom catalysts. *J. Am. Chem. Soc.* **141**, 14115–14119 (2019).
- Zhou, J. & Sun, Q. Magnetism of phthalocyanine-based organometallic single porous sheet. *J. Am. Chem. Soc.* **133**, 15113–15119 (2011).
- Marzari, N. & Vanderbilt, D. Maximally localized generalized Wannier functions for composite energy bands. *Phys. Rev. B* **56**, 12847–12865 (1997).
- Souza, I., Marzari, N. & Vanderbilt, D. Maximally localized Wannier functions for entangled energy bands. *Phys. Rev. B* **65**, 035109 (2001).
- Mostofi, A. A. et al. wannier90: a tool for obtaining maximally-localised Wannier functions. *Comput. Phys. Commun.* **178**, 685–699 (2008).
- Mathew, K., Kolluru, V. S. C., Mula, S., Steinmann, S. N. & Hennig, R. G. Implicit self-consistent electrolyte model in plane-wave density-functional theory. *J. Chem. Phys.* **151**, 234101 (2019).
- Mathew, K., Sundararaman, R., Letchworth-Weaver, K., Arias, T. A. & Hennig, R. G. Implicit solvation model for density-functional study of nanocrystal surfaces and reaction pathways. *J. Chem. Phys.* **140**, 084106 (2014).
- Bussi, G., Donadio, D. & Parrinello, M. Nosé-Hoover chains: the canonical ensemble via continuous dynamics. *J. Chem. Phys.* **126**, 2635–2643 (2007).
- Kuhne, T. D., Krack, M., Mohamed, F. R. & Parrinello, M. Efficient and accurate Car-Parrinello-like approach to Born-Oppenheimer molecular dynamics. *Phys. Rev. Lett.* **98**, 066401 (2007).
- Momma, K. & Izumi, F. VESTA: a three-dimensional visualization system for electronic and structural analysis. *J. Appl. Crystallogr.* **41**, 653–658 (2008).
- Peterson, A. A., Abild-Pedersen, F., Studt, F., Rossmeisl, J. & Nørskov, J. K. How copper catalyzes the electroreduction of carbon dioxide into hydrocarbon. *Energy Environ. Sci.* **3**, 1311–1315 (2010).
- Nørskov, J. K. et al. Origin of the overpotential for oxygen reduction at a fuel-cell cathode. *J. Phys. Chem. B* **108**, 17886–17892 (2004).
- Nørskov, J. K. et al. Trends in the exchange current for hydrogen evolution. *J. Electrochem. Soc.* **152**, J23–J26 (2005).
- Nørskov, J. K., Studt, F., Abild-Pedersen, F. & Bligaard, T. *Fundamental Concepts in Heterogeneous Catalysis*. (Wiley, 2014).
- Andreev, P. A. Separated spin-up and spin-down quantum hydrodynamics of degenerated electrons: spin-electron acoustic wave appearance. *Phys. Rev. E* **91**, 033111 (2015).
- Choy, T.-S., Chen, J. & Hershfield, S. Correlation between spin polarization and magnetic moment in ferromagnetic alloys. *J. Appl. Phys.* **86**, 562–564 (1999).

## Acknowledgements

The authors gratefully thank the International Science and Technology Cooperation Program (Grant No. 2017YFE0127800 and 2018YFE0203400), Natural Science Foundation of China (Grant No. 21872174 and U1932148), Hunan Provincial Science and Technology Program (Grant No. 2017XK2026), Shenzhen Science and Technology Innovation Project (Grant No. JCYJ20180307151313532), and Postdoctoral Research Fund of Central South University (Grant No. 140050047).

## Author contributions

M.L. and H.L. conceived the project, and K.L. demonstrated the idea and collected all the data. K.L. and J.F. wrote the paper. K.L., J.F., Y.L., T.L., G.N., and Z.L. analyzed the results. All authors read and commented on the manuscript.

## Competing interests

The authors declare no competing interests.

## Additional information

**Supplementary information** The online version contains supplementary material available at <https://doi.org/10.1038/s41467-022-29797-1>.

**Correspondence** and requests for materials should be addressed to Min Liu.

**Peer review information** *Nature Communications* thanks Jun Jiang and the other anonymous reviewer(s) for their contribution to the peer review of this work.

**Reprints and permission information** is available at <http://www.nature.com/reprints>

**Publisher's note** Springer Nature remains neutral with regard to jurisdictional claims in published maps and institutional affiliations.



**Open Access** This article is licensed under a Creative Commons Attribution 4.0 International License, which permits use, sharing, adaptation, distribution and reproduction in any medium or format, as long as you give appropriate credit to the original author(s) and the source, provide a link to the Creative Commons license, and indicate if changes were made. The images or other third party material in this article are included in the article's Creative Commons license, unless indicated otherwise in a credit line to the material. If material is not included in the article's Creative Commons license and your intended use is not permitted by statutory regulation or exceeds the permitted use, you will need to obtain permission directly from the copyright holder. To view a copy of this license, visit <http://creativecommons.org/licenses/by/4.0/>.

© The Author(s) 2022